A wind tunnel study of the aerodynamic characteristics of a scaled, aeroelastic, model tree

Hao, Yanfeng; Kopp, Gregory; Wu, Chieh-Hsun; Gillmeier, Stefanie

DOI:
10.1016/j.jweia.2019.104088

Document Version
Peer reviewed version

Citation for published version (Harvard):
Hao, Y, Kopp, G, Wu, C-H & Gillmeier, S 2020, 'A wind tunnel study of the aerodynamic characteristics of a scaled, aeroelastic, model tree', *Journal of Wind Engineering and Industrial Aerodynamics*, vol. 197, 104088. https://doi.org/10.1016/j.jweia.2019.104088

A wind tunnel study of the aerodynamic characteristics of a scaled, aeroelastic, model tree

Yanfeng Hao[1], Gregory A. Kopp[2,*], Chieh-Hsun Wu[2], Stefanie Gillmeier[3]
[1] Key Laboratory of Building Safety and Energy Efficiency of the Ministry of Education, Hunan University, Changsha, China, 410082
[2] Boundary Layer Wind Tunnel Laboratory, Faculty of Engineering, University of Western Ontario, London, ON, Canada, N6A 5B9
[3] Department of Civil Engineering, University of Birmingham, Birmingham, United Kingdom, B15 2TT

[*] Correspondence: Gregory A. Kopp
Email: gakopp@uwo.ca
Tel: 519-661-2111
Fax: 519-661-3339

Abstract

Tree crowns, unlike most bluff bodies, are both porous and flexible, so frontal area and crown deflection vary with wind speed. The former leads to aerodynamic force characteristics that vary with frontal area and wind speed while the latter is related to energy transfer between wind and tree. In order to investigate aerodynamic force characteristics and energy transfer, an approach to constructing an aeroelastic model of a tree, which satisfies geometric similarity, dynamic similarity and dimensionless parameters including Froude number, Cauchy number and density ratio, was developed and wind tunnel tests were carried out. The model was designed with eight distinct crown configurations according to different quantities of leaves. Aerodynamic forces, wind speed and frontal area were measured synchronously. The results showed that crown sheltering effects effectively limited mean crown deflection, which limit the mean base overturning moment coefficient. In addition, the energy transfer of the model with different crown configurations were investigated, and the characteristics of energy transfer were identified. It was shown that the crown frequency effectively controls the response via mechanical admittance, which amplified the response at the crown frequency.

Keywords

Tree aerodynamics; wind loads; aeroelastic modeling; wind tunnel methods.

Nomenclature

A_U	wind-speed-specific frontal area of the aeroelastic model tree
C1	configuration 1: trunk
C2	configuration 2: trunk and branches
C3	configuration 3: trunk and branches with 1 set of 90 leaf clusters
C4	configuration 4: trunk and branches with 2 sets of 180 leaf clusters
C5	configuration 5: trunk and branches with 3 sets of 270 leaf clusters
C6	configuration 6: trunk and branches with 4 sets of 360 leaf clusters
C7	configuration 7: trunk and branches with 5 sets of 450 leaf clusters
C8	configuration 8: trunk and branches with 6 sets of 540 leaf clusters
Ca	Cauchy number
C_M	base overturning moment coefficient
CS_{C_mU}	normalized co-spectral density function between base overturning moment coefficient and reference wind speed
CS_{MU}	normalized co-spectral density function between base overturning moment measured by force balance and reference wind speed
F_D	measured drag force in the direction of the wind flow
Fr	Froude number
d_{cc}	crown center displacement
D_{crown}	diameter of the crown projected to the ground
E	elastic modulus
f	frequency
f_{crown}	crown frequency
Fr	Froude number
g	gravitational acceleration
H	height of the model or the prototype
I_U	turbulence intensity
L	characteristic length
L_x	integral scale
M	base overturning moment measured by force balance
M_{qs}	estimated base overturning moment based on quasi-steady assumption
Re	Reynolds number
real(•)	real part
S_{aa}	power spectral density function of acceleration at the top of the trunk derived from free vibration decay tests
S_{CmCm}	power spectral density function of base overturning moment coefficient
S_{dccdcc}	power spectral density function of crown center displacement
S_{CmU}	cross spectral function between base overturning moment coefficient and reference wind speed
S_{MM}	power spectral density function of base overturning moment measured by force balance
$S_{M_{qs}M_{qs}}$	power spectral density function of estimated base overturning moment based on

		quasi-steady assumption
	S_{MU}	cross spectral function between base overturning moment measured by force balance and reference wind speed
	S_{UU}	power spectral density function of reference wind speed
	T	terrain configuration
	U	wind speed
	U_H	wind speed at the top of tree
	U_{ref}	reference wind speed at $z = 0.85\text{m}$
	$Var(\bullet)$	variance
	z	height above the wind tunnel floor
	z_{ref}	reference height in model scale or full scale
	δ_{model}	damping ratio of the model
	$\delta_{\text{prototype}}$	damping ratio of the prototype
	θ	momentum thickness of terrain configuration
	ν	kinematic viscosity of air
	ρ_{air}	air density
	ρ_{model}	model density
	$H(f)$	mechanical admittance function

1. Introduction

The magnitude of wind load is known to have a significant effect on trees. For example, it is known that relatively small wind loads over relatively long durations affect tree growth, while larger wind loads over short durations bring leaf loss or branch fracture and extreme wind loads bring stem breakage or uprooting (Robertson 1987). Different species of trees can experience different magnitudes of wind load under nominally similar wind conditions. This is mainly because the details of the crown, such as frontal area and flexibility of branches, are critical in setting the aerodynamic characteristics (Gillies et al., 2002; Tanaka et al., 2011; Cao et al., 2012). There are two main methods to study aerodynamic characteristics of trees. One is field measurements, which have mainly focused on the aerodynamic force coefficients (Grant and Nickling, 1998; Kane and Smiley, 2006; Kitagawa et al., 2015; Koizumi et al., 2010, 2016; Borisevich and Vikhrenko, 2018; Gonzales et al., 2018) and overall capacity (Gillies et al., 2000; Kane et al., 2008). Estimated aerodynamic forces acting on tree crowns obtained from field measurements are of value; however, are rarely conducted because of the obvious challenge. An alternative method that tends to focus on determining aerodynamic force coefficients relies on experimental modeling in wind tunnels (Mayhead, 1973; Vogel, 1989; Stacey et al., 1994; Gillies et al., 2002; Guan et al., 2003; Rudnicki et al., 2004; Vollsinger et al., 2005; Gromke and Ruck, 2008; Tanaka et al., 2011; Cao et al., 2012; Gromke, 2018). It is worth noting that Stacey et al. (1994) manufactured 12000 aeroelastic tree models to study wind flows and forces in a forest, in which the trees are somewhat simplified compared to full-scale prototype in order to achieve the objective of studying wind effects on a forest.

The two main wind tunnel approaches have been to use rigid models and dwarf potted trees. Rigid models cannot capture the shape changes due to branch and stem inflexibility. While dwarf potted trees capture flexibility effects; however these wind tunnel studies may not meet similarity

criteria because of mismatches between stem, branch and leaf sizes. This makes it challenging to transfer the measured results into full-scale dimensions for high wind speed ranges (Gromke and Ruck, 2008). A hybrid of the two aforementioned approaches is to use very large wind tunnels with small, but full-scale, trees. Some of these tests have ignored the effects of turbulence in the atmospheric boundary layer (Mayhead, 1973; Aly et al., 2013), which limits the usefulness of the results. However, more recent studies have also included gust effects (Miller et al., 2015; Giammanco et al., 2016). Therefore, the first objective of the study is to develop an approach to constructing an aeroelastic model of a tree with different crown configurations which satisfies the geometric similarity, dynamic similarity and dimensionless parameters including Froude number, Cauchy number and density ratio on the base of filed measurement, and use multiple turbulence profiles in order to show their effects.

The classical formula for drag, F_D, in the direction of wind flow on a bluff body is

$$F_D = \frac{1}{2} C_D \rho A U^2 \quad (1)$$

where C_D is the drag coefficient, ρ is the air density, A is the frontal area, and U is the wind speed. For a rigid bluff body, the frontal area does not vary with wind speed; however, this is not the case for trees, which change shape with wind speed, as discussed above. Crown streamlining is defined as the tendency of leaves and branches to align with the wind direction. Because this has the effect of decreasing the frontal area of the crown, the frontal area as a function of wind speed needs to be measured. Rudnicki et al. (2004) found that crown streamlining effects reduce the frontal area of conifer species by 36% to 54% at 20 m/s. Vollsinger et al. (2005) also found that this effect decreases the frontal area of hardwood species to about 20% to 37% of their initial values at 20 m/s. These results indicate that crown streamlining is a key factor for the frontal area under wind load.

Prior to the 21st century, frontal area measurements were mainly obtained via photography and tended to focus only on mean values or singular moments in time. Mayhead (1973) was the first to estimate frontal area through photography. Vogel (1989) used an area meter, which was a geometric figure of accurately known area, to measure leaf area. Since the beginning of the 21st century, digital photography has transformed the methods for identifying frontal area. With this technique, frontal area is calculated by counting pixels using gray scale images (Gillies et al., 2002; Rudnicki et al., 2004; Vollsinger et al., 2005; Cao et al., 2012; Gonzales et al., 2018). Although this research has provided significant contributions in estimating the frontal area, time dependent measurements are lacking, which limits the ability to model the gust effects caused by turbulence. Therefore, the second objective of the study is to use high frequency camera to record and analyze time histories of the frontal area and the crown deflection under wind load.

Aerodynamic force coefficients mainly depend on aerodynamic shape, surface roughness, and inflow turbulence. For flexible bodies, they also depend on the motion. For bluff bodies at high Reynolds numbers, aerodynamic force coefficients are usually fairly constant (Vogel, 1989). However, this does not appear to be the case for trees because of the porous structure and the changing geometry with wind speed due to crown streamlining. For example, Mayhead (1973) found that mean drag coefficients of trees decrease with increasing wind speed. This result has been validated by Rudnicki et al. (2004), Vollsinger et al. (2005) and Cao et al. (2012). Vogel (1989) found that drag coefficients of leaves decrease with increasing wind speed. Clearly, frontal area, wind speed and aerodynamic force coefficients affect each other. However, it is difficult to

measure fluctuations of these parameters synchronously, which limits accurate modeling of overall wind loads using dynamic models. Therefore, the third objective of the study is to measure the responses of the aeroelastic model tree including the frontal area, wind speed and aerodynamic forces simultaneously, and study the effects of numbers of branches and leaves on the mean and fluctuating values of aerodynamic forces, crown deflections, and the frequency content of these parameters.

Gardiner (1994) regarded the tree as a linear system and studied the transfer function between wind speed and tree displacement by field measurements. Moore and Maguire (2008) use finite element analysis to calculate the similar transfer function for trees. Such research has provided significant contributions regarding the energy transfer in trees. However, crown configurations for trees are always changing because of the seasonal effect on leaves. Therefore, the fourth objective of the study is to use the obtained data for different crown configurations to study the effects of different numbers of branches and leaves on energy transfer function.

The layout of this paper is as follows. The aeroelastic model tree, terrain simulation, measurements and instrumentation are described in Section 2. Section 3 presents the aerodynamics of the aeroelastic model tree, Section 4 presents the dynamic response of the aerodynamic model tree, while Section 5 presents energy transfer (mechanical admittance). Finally, conclusions are offered.

2. Materials and methods

2.1 Design of the aeroelastic model tree

2.1.1 Overview of dynamic similarity requirements

The prototype for the study is a camphor tree (*Cinnamomum camphora*), which is broad-leaved and located widely in the south of China. Flexible structures, such as a tree, require matching several non-dimensional parameters in order to achieve dynamic similarity. These are summarized in Table 1. In addition to geometric similarity, an aeroelastic model should match the full-scale values of the following dimensionless parameters:

- Density ratio $(\rho_{model}/\rho_{air})$;
- Froude number $(\mathrm{Fr} = U^2/gL)$;
- Reynolds number $(\mathrm{Re} = UL/\nu)$;
- Cauchy number $(\mathrm{Ca} = \rho U^2/E)$;
- Damping ratio $(\delta_{model}/\delta_{prototype})$ (Holmes, 2001).

The geometric scale of the aeroelastic model was chosen to be 1/6. This scale was mainly chosen to meet the requirement of the blockage ratio to be below about 5% while having a Reynolds number as large as possible because of the circular cross-sections of the branches and trunk, and noting that Reynolds number cannot typically be matched for scale model testing. The scale of the atmospheric boundary layer also needs to match this geometric scale, a point which is discussed further below.

Density ratio and length scale determine the model mass. Because of the use of a wind tunnel to simulate the natural wind, the air density of the prototype and the model are the same. This then leads to the requirement that the densities for the prototype and model components are the same. The current model had both the correct total mass and the distribution placed correctly.

The Froude number is a dimensionless parameter that represents the ratio of inertial to gravitational forces. Because of the importance of both gravitational and inertial loads on the

branches, crown, and trunk, matching the Froude number is required. This parameter is generally required in full aeroelastic model testing of long-span bridges and cable-suspended roofs (Holmes, 2001). Once the length scale is set, matching the Froude number leads to the velocity scale requirements, which becomes the square-root of the length scale (because the gravitational constant is fixed). Of course, once the length and velocity scales are fixed, the time (or frequency) scaling is also set.

On the other side, once the geometric and velocity scales are fixed in the wind tunnel, the Reynolds number is also set. Reynolds number similarity is not possible in most cases for boundary layer wind tunnels, as noted above. However, because the velocity scale is 1:2.45 and the length scale is 1:6, the model-scale Reynolds number is only a factor of 15 lower than full-scale. This may have some effect on the results, although the circular surfaces were roughened to minimize these.

The Cauchy number is a dimensionless parameter that represents the ratio of the inertia forces to the elastic forces. Here, we scaled the bending stiffness instead of the elastic modulus. Bending stiffness is the product of elastic modulus and second moment of area. Cauchy number is a difficult parameter to scale because of limitations in the availability of materials. In this case, modelling the stiffness of a branch or stem leads to significant challenges, which are discussed further below.

Finally, the damping ratio plays a key role in the dynamic response. The adjustment of the damping ratio is not straightforward to control in aeroelastic models generally and is difficult to determine in natural structures such as tree. This is mainly because collisions among branches and leaves contribute significantly to the damping of tree, and these random collisions cannot be controlled effectively and independently in the model tree with the approach to the numerous branches and leaves. The damping of the prototype is 5.4% based on modal measurements in the field, as described in Section 2.1.3. This damping, which is called “internal damping”, arises from two sources: the friction of the root-soil connection, and structural damping resulting from the movement of branches and the internal friction of the wood (Moore and Maguire, 2004). Although the damping of the aeroelastic model is about 2%, this discrepancy is not unexpected. In particular, it is reasonable that the damping of the model is smaller than the prototype because the model is fixed to the ground and the damping does not include the contribution from the friction of the root-soil connection. However, it is difficult to determine how much the friction of the root-soil connection of the prototype contributes to the damping. This mismatch will cause some discrepancy of the swaying behavior.

2.1.2 Description of the aeroelastic model tree

Camphor trees are widely used as raw materials for medicine and furniture (Hu et al., 2012). A transplanted camphor tree (which was transplanted 2 years prior to analysis) was selected as the prototype of the aeroelastic model tree. The main dimensions, including trunk height, trunk diameters at different heights, crown height, crown diameter, diameters and inclinations of main branches, and leaves, were measured by gradienter, vernier caliper and laser range finder. Based on these sizes, the tree skeleton (Figure 1b) was extracted from the prototype (Figure 1a) and the physical model (Figure 1c) recovered. The dynamic characteristics of the prototype were measured in field, which are discussed further in Section 2.1.3. The physical parameters of the trunk and branches of the prototype, including density and elastic modulus, were derived from the

method of Jiang and Peng (2001). The resulting designs of each component of the model tree are described below.

The trunk model borrows from the method of full aeroelastic model of long-span bridges. The structural skeleton of the trunk is made of a high-strength aluminum rod ($\rho = 2700\mathrm{kg/m^3},\ E = 6.91 \times 10^{10}\mathrm{Pa/m^2}$) of circular cross section, which is 0.5m long. In addition to diameter at breast height (DBH = 0.15m), the diameters at 15 distinct heights of the prototype trunk were also measured. Based on these sizes, the aluminum spine was machined so that the variation of trunk diameter on the model stiffness was modelled. Such variation is important in modelling the bending responses. The connection at the top of the trunk was designed to provide a fixed joint for branches. In order to simulate the aerodynamic shape of the trunk, 15 segments of "cladding components" were attached to the trunk spine. Adjacent segments were separated by a 0.8 mm gap in order to prevent their contacting each other with a subsequent contribution to the trunk stiffness. These were 3D printed to have the correct mass by adjusting the "wall" thickness.

There were 10 main "first-class" branches and 102 "higher-class" branches to support the crown frame. The method used to build the trunk was not suitable for making aeroelastic branches because the diameters of the branches are too small at a scale of 1:6 (ranging from 0.003 - 0.009 m). As an alternative, a combination of aluminum wire ($\rho = 2700\mathrm{kg/m^3},\ E = 6.91 \times 10^{10}\mathrm{Pa/m^2}$) and rigid hollow rods ($\rho = 930\mathrm{kg/m^3}$) was used, based on the principle of equivalent mass and displacement. To describe the concept of equivalent displacement, the true deformation of an aeroelastic branch (Figure 2a) is replaced by the alternative model (Figure 2b). One obvious distinction is that the aeroelastic branch deformation is curved while the alternative deformation is a combination of curve and linear. Although it may affect local displacements of branches, crown streamlining of branches of two models would be consistent, because the free ends of the branches of the two models have the same displacement under the same load. Based on this, the stiffnesses of the two models are the same. The appropriate mass of the model is obtained by altering wall thickness of the hollow rod, so that the resulting natural frequencies match those of the prototype.

The range of leaf mass was determined by comparison between natural frequency of the prototype measured in field and that of a finite element model in which leaf weight can be adjusted to match the natural frequency. Because the field measurements happened during autumn, considering the seasonal effect on leaves, this mass range was altered suitably so that the natural frequency and crown area of the model were in the range of the prototype over the course of a year. There were 540 leaf clusters in total added to the model, which is much smaller than for the prototype over much of the year. Based on the fact that the typical leaf cluster of the prototype usually includes 5 leaves (Figure 3a), model leaf clusters (Figure 3c) were made according to a computer-based 3D model of a leaf cluster (Figure 3b).

Leaves are made of lamina and petiole. Lamina determines leaf deformation while petiole determines leaf direction (Vogel, 1989). Dynamic characteristics of leaves were neglected because of material limitations: sheet plastic and steel piano wire were used to model the lamina and petiole, respectively. Because the clusters are made of steel piano wire and sheet plastic, the stiffness of man-made cluster is larger than the prototype, which causes different deformations and directions of the leaves between the prototype and the model under wind load. This is a limitation of the model, which needs to be addressed in the interpretation of the results.

Eight crown configurations of the aeroelastic model were designed by assembling different

quantities of branches and leaf clusters. These include the trunk portion of the model tree, which is named as case C1 (Figure 4a). Case C2 (Figure 4b) includes both trunk and branches. Case C3 is formed by adding one leaf cluster to each of the branches in case C2 (Figure 4b). Following the same way, the branches were incrementally added with clusters for cases C4 to C8 shown in Figures 4d-h, respectively. Six sets of clusters were incrementally increased in order from free-ends to fixed-ends of branches to simulate the growth sequence of leaves in reality. The dimensions and mass of eight configurations of the aeroelastic model tree are listed in Table 2.

2.1.3 Dynamic characteristics of the aeroelastic model tree

For the accurate identification of the natural frequencies of the aeroelastic model tree, a modal analysis using a finite element model (FEM), along with experimental displacement tests of the model tree were conducted. The former was accomplished using the ANSYS finite element software package according to the dimensions and material properties of the aeroelastic model tree (Figure 5a). The latter was completed by free vibration decay tests of the trunk. For the experiments, the crown was released from a relatively large displacement within the elastic range of the materials in order to increase collisions among branches and leaves as much as possible in the process of free vibration. Then, the free vibration decay time history was recorded by a high sensitivity accelerometer attached to the top of the trunk. Figure 5(b) illustrates the overall mode shape at $f = 2.0$ Hz for case C8, in which all branches sway in phase, but without trunk swaying. This frequency is close to the frequency range where the first peaks are identified in the power spectral density functions of the acceleration atop the trunk (Figures 5d, e). Based on these characteristics, this frequency range is defined as the "crown frequency". In addition, based on case C1 (just the trunk without the crown; Figure 4a), and the continuity of frequency variation of the trunk (from cases C1 to C8) shown in Figure 5(d) and (e), this frequency range is defined as the "trunk frequency". Figure 5(c) illustrates the overall mode shape at the trunk frequency range ($f = 12.2$ Hz) for case C8, in which trunk sways out of phase with crown.

Figure 5(f) shows frequencies of the aeroelastic model for the eight crown configurations in the two orthogonal directions. The crown frequency, which is far smaller than trunk frequency, as shown in the Figure 5(f), indicates that the crown with a spreading canopy and no central trunk sways as a whole (James, 2010). The collisions among branches and leaves are key factors in this process. In addition, crown frequency is also governed by the stiffness and mass of branches, along with the leaf mass. The crown vibration is more obvious than trunk vibration in this frequency range (Figure 5b). Crown frequencies in the along-wind direction are almost the same as those in the across-wind direction, which indicates the symmetry of the model. Crown frequencies decrease with increasing numbers of leaf clusters (Figure 5f) because of the added mass.

On the other hand, trunk frequency depends on the stiffness and mass of the trunk and crown. The trunk frequency of the prototype camphor tree was identified by modal measurement method of Single Input Single Output (SISO). This method measures response at one fixed point of the trunk while lightly hitting different points along the height of the trunk with a force hammer (Reynders et al., 2010). The trunk frequency of the prototype is found to be 5.18 Hz. Based on the frequency scale of 2.45:1, the target frequency of the model trunk is 12.68 Hz. Trunk frequency of C6 is 12.70 Hz (Figure 5f), which is reasonably close to the target trunk frequency (i.e., 0.2% higher).

The ratio between the crown and trunk frequencies for different crown configurations is about 1:3 to 1:4. Serigo et al. (2008) found that the ratio of the first two frequencies of an olive tree with a spreading canopy and no central trunk is about 1:2. Schindler et al. (2010) found that the ratio for a plantation-grown Scots tree with a central trunk is about 1:3. These indicate that the first two frequencies of the aeroelastic model tree are reasonable.

2.2 Terrain simulation

The turbulent atmospheric boundary layer (ABL) flows were simulated in the high-speed section of the Boundary Layer Wind Tunnel Laboratory (BLWTL) II at University of Western Ontario (UWO), Canada. It has a fetch of 39 m for flow development. The cross section at the test location is 3.36 m wide and 2.05 m high. Three spires with 1.22m height and 0.1 m base width were placed at the upstream inlet. Sets of roughness blocks are distributed along the fetch between the inlet and the test location. By altering the heights of roughness blocks and barriers, four different ABL flows (T1-T4) were generated.

Mean wind speed profiles were measured using a Cobra Probe (TFI, Model no. 900, 311) at a sampling frequency of 625 Hz. In what follows, the ABL flow conditions to which the aeroelastic model tree was exposed are described in detail. Therefore, mean wind speeds and turbulence intensities of the ABL flows simulated with terrains T1-T4 are analyzed. Vertical profiles of the aforementioned ABL flows are shown in Figure 6. In addition, ESDU 85020 (2008a) guideline is used to illustrate flow characteristics of two full-scale ABL flows which develop as a result of "open" (T5) and "suburban" (T6) terrains. While the mean velocity profiles of T1, T2 and T3 are similar to that of T5 for heights similar to the crown height, the velocity profile of T4 differs at all heights investigated, which indicates that wind tunnel terrains provide realistic bounds on full-scale terrains in the mean flow sense. There is a clear increase in turbulence intensities ($I_{U,T1} < I_{U,T2} < I_{U,T3} < I_{U,T4}$) from terrain T1 to terrain T4. While turbulence intensities of T4 are similar to those obtained for terrain T5, turbulence intensities of terrain T6 are the largest among the different ABL flows investigated. This finding may suggest that gust effects are underestimated for measurements conducted for terrains T1-T3. Table 3 provides turbulence intensities at the reference height ($z_{ref} = 0.85\mathrm{H}$) for all terrain types investigated.

Figure 7 shows plots of power spectral density functions of streamwise velocities for all six ABL flows at corresponding measurement heights, namely, at $z_{ref} = 0.85\mathrm{m}$ for terrains T1 - T4 and at $z_{ref} = 5.1\mathrm{m}$ for terrains T5 and T6. The power spectra of terrains T1-T4 illustrated in Figure 7 shows that the magnitudes of the measured power spectra seem to be primarily dependent on the turbulence intensity; the magnitude increases with increasing turbulence intensity. Figure 7 furthermore illustrates the power spectral density functions of terrains T5 and T6, and thereby highlights large differences between the power spectra of terrains T1-T4 and T5-T6. Table 3 shows that the dimensionless integral length scale (L_x/D_{crown}) of terrains T5 and T6 are significantly larger compared to those obtained for terrains T1-T4, which is caused by the primary issue when using relatively large scale models in typical boundary layer wind tunnels. The mismatch of integral length scales causes the tree's crown to miss the response caused by relatively large scale wind gusts. As a result, investigations conducted with terrains T1-T4 will likely underestimate the tree's response compared to full-scale. Momentum thicknesses normalized by the height of the model tree, $\theta/H, \theta = \int_0^H \frac{U}{U_H}\left(1 - \frac{U}{U_H}\right) dz$, are shown in Table 3.

The momentum thicknesses of terrains T5 and T6 lie within a similar range as terrains T1-T4, which indicates that the analyzed terrains will not miss the effects caused by momentum thickness.

2.3 Measurements and instrumentation

The wind tunnel tests were carried out in BLWTL II at UWO. The set-up of the wind tunnel tests and coordinate system definition are shown in Figure 8. Aerodynamic forces, wind speed, and crown area were measured synchronously to determine characteristics of aerodynamic forces, aerodynamic force coefficients and crown deflections, and energy transfer functions.

Aerodynamic forces were measured by a six-component force balance (JR3, Model no. 5640). Background noise of the force balance is typically less than 4% of the measured coefficients of variations (COV) with the wind. Because aerodynamic forces caused by the crown dominate the total aerodynamic forces of the tree, four cobra probes are used to measure the local wind speed around the crown. The locations of the four cobra probes are shown in Figure 8. Cobra probe 1 was used as reference wind speed to calculate aerodynamic force coefficients. The data for aerodynamic forces and wind speeds were collected synchronously at a sampling rate of 625 Hz for a duration of 245 s, which relates to approximately 10 minutes in full-scale.

Two 1 Mb Photron FASTCAM-1024 PCI CMOS cameras (maximum sampling frequency: 1000 Hz) were used to record digital images of the aeroelastic model. A more detailed description of the cameras can be found in Taylor et al. (2010). Two digital cameras were installed: one downstream of the aeroelastic model and the other one at the side of the model, as can be seen in Figure 8. These cameras were used to capture images to calculate frontal area and crown deflection during each run at a sampling rate of 60 Hz for 20 s, which is sufficient to resolve all dynamic effects. Images from both cameras were synchronized in time with the aerodynamic force and wind speed measurements.

Figure 9(a) shows that compared to the dark wind tunnel background, the model tree is shown white on the gray-scale images. For the digital image processing, first, a threshold was defined by means of which a program could determine whether pixels in the gray-scale image are counted as white (tree) or black (no tree). Within this process, all “tree pixels” were assigned a bright white color, as shown in Figure 9(b). The frontal area of the tree was then estimated by counting the number of white pixels in the processed image. In this processing, the reference scale (6.818×10^{-7} $\mathrm{m}^2/\mathrm{pixel}$) between pixel size and length was determined by a calibration block in the image. In order to enhance the accuracy of determining the frontal area, the contrast between tree and background was increased by covering components that reflected light in black tape and lighting only the test section of the wind tunnel while turning off all other lights.

The identification of crown deflection follows a similar method as described for the frontal area. Firstly, the crown center, which is defined as the center of mass of all white pixels, was identified. The reference crown center was calculated without wind, and by subtracting the location of the reference crown center from the location of the deflected crown center (due to wind), the crown's displacement due to wind was obtained.

The process for recording data is described as follows. Still images of the aeroelastic model were first captured from both cameras to calculate the frontal area and the original position in still air. Then, the wind speed was increased to the desired level and the measurements of images, wind speeds, and base reactions were conducted synchronously. The aeroelastic model tree was

subjected to six different average reference wind speeds (nominally about 3.7, 4.6, 5.6, 6.7, 7.8 and 8.8m/s). The Reynolds numbers based on the average trunk diameter and these wind speeds range from 6,200 to 14,700.

3. Aerodynamics of the aeroelastic model tree

3.1 Mean base overturning moments

The trunk is usually described as a cantilever fixed perpendicularly to the ground. Trunk breakage is usually caused by large tensile stresses that occur when the bending moment and self-weight exceed the tensile strength of the trunk. In this failure mode, the bending moment plays a key role. The base overturning moment caused by crown mass and crown displacement is separated to obtain the purely aerodynamic moment. The corresponding base overturning moment coefficient is defined as

$$C_M = \frac{M - m_{crown} * d_{cc}}{0.5 \rho U_{ref}^2 A_U H} \quad (2)$$

where C_M is the base overturning moment coefficient, M is the base overturning moment measured by the force balance, m_{crown} is the crown mass corresponding to the different configurations, d_{cc} is the crown center displacement, ρ is the air density, A_U is the wind-speed-specific frontal area, which is defined as frontal area corresponding to mean reference wind speed and crown configuration, U_{ref} is the reference wind speed, and H is the height of the aeroelastic model tree. For the mean base overturning moment coefficient, $\bar{C}_M$, mean values are used for all time-varying quantities in equation (2). For time-varying analyses of C_M, simultaneously measured time-varying quantities are used in equation (2).

Figure 10(a) shows the relationships between frontal area and reference wind speed in terrain T1. For the different crown configurations, frontal areas are essentially constant with wind speed and depend on the number of leaves included in the crown configurations, ranging from 0.05 to 0.14 m^2 (model scale) for cases C2 to C8, which indicates that it has little effect on base overturning moment coefficient. Thus, crown streamlining effects are not observed directly with this model. We attribute this to the excess stiffness of the model lamina and petiole, as indicated in Section 2.1.2.

The effects of crown configuration and wind speed on the mean base overturning moment coefficient in terrain T1 are shown in Figure 10(b). The different values along the abscissa in the Figure 10(b) are determined by different crown configurations. The mean base overturning moment coefficients increase with increased numbers of leaf clusters and tend to be steady when there are relatively more leaf clusters (for case C8). This is mainly because the initial increased number of leaves significantly change the aerodynamics of the model tree. This leads to increased base overturning moment coefficients. The steady trends are mainly caused by crown deflection, and not by frontal area, because frontal areas are basically constant with wind speed (Figure 10a), and crown center displacements are consistent with the increasing trends followed by steady trends for base overturning moment coefficients, which are discussed later in the paper (Figure 15a). At the same time, the mean base overturning moment coefficients decrease for larger wind speeds, which is discussed further in Section 3.2. This result is also found in wind tunnel tests of broad-leaved species (Cao, et al., 2012; Vollsinger, et al., 2005) and field measurements of broad-leaved species (Kitagawa, et al., 2015; Koizumi, et al., 2010).

Figure 11 shows the effects of the ABL momentum thickness on the mean base overturning

moment coefficient. For a specific crown configuration, it can be seen that the mean base overturning moment coefficients are basically constant in the range of momentum thickness from 0.07 to 0.10, associated with the smoother terrain T1, T2 and T3, and then decrease for 0.17, which represents the rougher terrain T4. This is mainly because momentum thickness is a parameter which reflects the differences in the mean wind speed profile. Increased momentum thickness corresponds to reduced mean wind speeds in the profile, which reduces the aerodynamic forces acting on the tree.

3.2 Fluctuating base overturning moments

In order to determine fluctuating characteristics of base overturning moments and moment coefficients, various statistical parameters were investigated for cases C2 to C8. Table 4 provides the mean values, standard deviations (SD) and COV of reference wind speeds, base overturning moments, and moment coefficients in terrain T1. The COV for the base overturning moments decrease from 12% to 8% for the increased numbers of leaves (for cases C2 to C8), with turbulence intensities hold constant at about 6%, even though both the mean and fluctuating (SD) of the base overturning moments increase substantially with increased numbers of leaves. It is not clear what causes this, because there is no apparent correlation between COV of base overturning moments and damping (including both structural and aerodynamic damping; Table 4), which is derived from crown deflection calculated by both the random decrement method and the logarithmic decrement method (James, 2010). In contrast, the COV for the base overturning moment coefficients fluctuate around the average value about 14% for the different crown configurations (with turbulence intensities hold constant at about 6%). Further analyses will be presented below and in the following sections.

Figures 12(a) and (b) show the effects of turbulence intensity (in terrain T1, T2, T3 and T4) on the COV for the base overturning moments and moment coefficients, respectively. The COV for the base overturning moments increase linearly with larger values of turbulence intensity (Figure 12a). It is worth noting that the increased numbers of leaf clusters tend to slightly mitigate the fluctuations of base overturning moments. The COV for the moment coefficients as a function of turbulence intensity exhibit similar trends, although the frontal area has some effect on the normalized response.

The characteristics in frequency domain about base overturning moment are described in Figure 13. Figure 13(a) illustrates the power spectral density functions of the base overturning moments for cases C2 to C8 in the along-wind direction at the reference wind speed of 8.8 m/s in terrain T1. The broad peaks for base overturning moments are identified to be close to the crown frequency. The secondary peaks, which are relatively smaller in magnitude and narrower in bandwidth, are identified to be in the range of the trunk frequency (Figure 5f). These indicate that crown frequencies dominate the fluctuations of the base overturning moments. Figure 13(b) show the similar results for the base overturning moment coefficients. Figure 13(c) illustrates the power spectral density functions of the base overturning moment coefficients for case C8 at the reference wind speeds of 3.7 to 8.8 m/s at same conditions. The broad peaks for different wind speeds are constant and identified to be close to the crown frequency, which indicates that the base response is determined by crown frequency and not related to a possible vortex induced vibration.

The normalized co-spectral density function in the along-wind direction is defined as (Holmes,

2001)

$$CS_{MU} = \text{real}(S_{MU}/\sqrt{S_{MM} * S_{UU}}) \quad (3)$$

$$CS_{C_mU} = \text{real}(S_{C_mU}/\sqrt{S_{C_mC_m} * S_{UU}}) \quad (4)$$

where CS_{MU} is the normalized co-spectral density function between the base overturning moment (measured by the force balance) and the reference wind speed, while CS_{C_mU} is the normalized co-spectral density function between base overturning moment coefficient and reference wind speed. S_{MU} is the cross spectral function between the base overturning moment (measured by the force balance) and the reference wind speed, S_{C_mU} is the cross spectral function between the base overturning moment coefficient and the reference wind speed, S_{MM}, $S_{C_mC_m}$, S_{UU} are the power spectral density functions of the base overturning moment (measured by the force balance), base overturning moment coefficient and reference wind speed, respectively, and $\text{real}(\bullet)$ is real part. The time history of the base overturning moment coefficient is calculated by equation (2), which is determined by the fluctuations of the base overturning moment (measured by the force balance), reference wind speed and frontal area.

The details of the correlation between the wind speed fluctuation and the base overturning moment are described in Figure 14. Subplot (a) in Figure 14 shows a 3-sec time segment of the normalized velocities and base overturning moment fluctuations (i.e., $(U(t+\tau)-\bar{U})/(U'^2)^{0.5}$ and $(M(t)-\bar{M})/(M'^2)^{0.5}$) in terrain T1. Because the velocity probe is placed a short distance upstream of tree model (Figure 8), the velocity signal shown in Figure 14(a) is delayed by a lag time, τ, for better visual comparison with the moments. Figures 14(b) shows the corresponding base overturning moment coefficients by using the two quantities in Figure 14(a), i.e., $C_M(t) = (M(t) - m_{crown} * d_{cc})/(0.5 * \rho * U_{ref}(t+\tau)^2 * A_U(t) * H)$. Figure 14(c) further shows the co-spectra to quantify the correlation (in the frequency domain) between velocity and base overturning moment, while Figure 14(d) shows the co-spectra for the velocity and moment coefficients.

From Figure 14(a), it is clear that the large-scale turbulence (i.e., slowly varying wind speed traces) correlates well with base overturning moment responses, while the pattern of the small-scale turbulence (i.e., fast-changing velocities) are not found in the base overturning moments. This observation is consistent with the co-spectral plot shown in Figure 14(c), in which the correlation coefficients reach a maximum (of about 0.5) at frequencies lower than the crown frequency, and decay to zero for frequencies larger than crown frequency. This is mainly because, at frequencies lower than the crown frequency, the base overturning moment of the model is basically determined by the large-scale gust, and the model is behaving in quasi-steady manner. The sudden drop of the co-spectra at the crown frequency is thought to be induced by the mismatch of random turbulent fluctuations and the regularized crown vibration.

From the co-spectra plot shown in Figure 14(d), however, negative correlations can be found between the velocity fluctuations and the base overturning moment coefficients. Because the moments are nearly unresponsive to small-scale turbulence (i.e., for $f > f_{\text{crown}}$), as already

shown in Figures 14(a) and (c), a positive small-scale gust means a direct increase of the denominator in Eq. (2), and, hence, a direct decrease of moment coefficient. The examples of these situations are labeled as blue boxes in Figures 14(a) and (b), which provides the explanation for the negative correlation between small-scale gusts and moment coefficients. On the other side, Figure 14(d) implies a negative correlation between the large-scale gust (i.e., $f < f_{\mathrm{crown}}$) and base overturning moment coefficients. This is further asserted by looking at the yellow-circled region of the time histories shown in Figures 14(a) and (b), in which the stronger gust is associated with lower moment coefficient, and vice versa. Note that this observation also echoes the negative correlation between mean velocity and mean base moment coefficients in Figure 10(b).

To explain the negative correlation between the (large-scale) gust and the base overturning moment coefficient, the side-view snapshot of the tree model taken at a time, τ, after the peak positive gust is shown in Figure 14(e) and compared to that corresponding to a negative gust shown in Figure 14(f). It is clear that the crown is displaced more into the stream direction for the positive gust. Such an instantaneous shape is thought to be more aerodynamic than the shape associated with the negative gust, and, hence, reduces the base moment coefficients for the positive gust. This mechanism is postulated to explain the negative correlation between the large-scale turbulence and the base overturning moment coefficient.

4. Dynamic response of the aeroelastic model tree

4.1 Mean crown deflections

The crown center displacement is a primary parameter to evaluate crown deflection. The effects of crown configuration and wind speed on mean crown center displacements in the along-wind and across-wind directions in terrain T1 are shown in Figures 15(a) and (b). Figure 15(c) depicts the relationships between mean crown center displacements and mean base overturning moment coefficients for different reference wind speeds in terrain T1. The monotonically increasing trends for crown center displacements in the along-wind direction cease at about $\bar{A}_U^{0.5}/H \approx 0.34$, which are followed by stable trends for $\bar{A}_U^{0.5}/H \approx 0.37$. This is mainly because, as the number of leaves is increased from zero, the area that the wind can act on directly is also increased, which leads to increased aerodynamic forces. This causes increased crown center displacement. However, for crown configurations with larger numbers of leaves and branches, sheltering effects play an important role in reducing the relative importance of further increased quantities of leaves and branches such that the crown center displacement tends to level off with increased area, which indicates that some branches and leaves are sheltered from each other under wind load. In fact, the current study indicates that up to 33% of the leaves (relative to case C8) can be removed without affecting the crown center displacement. The crown center displacements in the along-wind direction clearly increase with increasing the reference wind speed, as expected. The relationships between mean crown center displacements and mean base overturning moment coefficients present similar changes. These can be explained by the crown sheltering effects. The crown center displacements in the across-wind direction are far less than these in the along-wind direction, which indicates that the crown response in the along-wind direction dominates crown behavior in windy conditions.

4.2 Fluctuating crown deflections

In order to determine fluctuating characteristics of the crown center displacements, the COV

and power spectral density functions were obtained from the time histories of crown center displacements in the along-wind and across-wind directions for cases C2 to C8.

Table 4 shows the mean values, SD and COV of reference wind speeds and crown center displacements in the along-wind and cross-wind directions in terrain T1. There is a decreasing trend of the COV of crown center displacements in the along-wind direction from 10% to 6% for increased numbers of leaves, with turbulence intensities hold constant at about 6%. However, the COV of crown center displacements in the across-wind direction are much larger than those in the along-wind direction. This is mainly because the crown center displacements in the across-wind direction fluctuate about zero, and noting that the variance is about two thirds of that for the along-wind direction. This is likely a reflection of the differences between the longitudinal and lateral turbulence intensities.

Figure 16 shows the effects of turbulence intensity (in terrain T1, T2, T3 and T4) on the COV for the crown center displacements in the along-wind direction. The relationships are observed to be similar as those between the base overturning moments and turbulence intensity. There is a similar slight reduction in the COV for the crown center displacements with larger numbers of leaf clusters.

The vibration characteristics in frequency domain about crown center displacement in orthogonal directions are described in Figure 17. Figures 17(a) and (b) show the power spectral density functions of the crown center displacements in the along-wind and across-wind directions for cases C2 to C8 at reference wind speed of 8.8 m/s in terrain T1. The frequency range where the main peaks for the crown center displacements in both two directions are located is close to the crown frequency range. The secondary peaks in the trunk frequency range are less significant, indicating that the crown frequencies dominate the fluctuations of the crown center displacements and not the trunk fluctuations. Figures 17(c) and (d) show power spectral density functions of the crown center displacements in the two directions for case C8 at reference wind speeds of 3.7 to 8.8 m/s at same conditions. The constant frequency where the main peaks are located indicates crown deflection is not related to a possible frequency of vortex shedding.

5. Energy transfer (mechanical admittance)

Based on quasi-steady assumption, the base overturning moment is estimated:

$$M_{qs} = 0.5\rho \bar{C}_M U_{ref}^2 \bar{A}_U H \tag{5}$$

The mechanical admittance function in the along-wind direction is defined (Davenport, 1963)

$$S_{MM}(f) = |H(f)|^2 S_{M_{qs}M_{qs}}(f) \tag{6}$$

Where M_{qs} is estimated base overturning moment based on the quasi-steady assumption, $S_{MM}(f)$ is the power spectral density function of base overturning moment measured by the force balance, $S_{M_{qs}M_{qs}}(f)$ is the power spectral density function of estimated base overturning moment based on the quasi-steady assumption, and $H(f)$ is the mechanical admittance function.

In fact, the mechanical admittance based on the quasi-steady assumption that aerodynamic force fluctuations are determined by the turbulent fluctuations of the wind is the combination of aerodynamic and mechanical admittance. To separate the aerodynamic admittance, wind tunnel tests with a rigid model would be necessary. Therefore, a general experimental formula for

aerodynamic admittance, $\chi(f) = 1/(1 + \left[\frac{2f\sqrt{\bar{A}_U}}{\bar{U}_{ref}}\right]^{4/3})$ (Holmes, 2001), is included to provide a reference for "typical" characteristics (Figure 18). It is generally accepted that for large-scale gusts, that the aerodynamic admittance is 1 since quasi-steady theory will tend to hold for these relatively slowly changing wind speeds. In contrast, the overall loads are not affected significantly by the smaller-scale turbulence so the admittance falls off rapidly at high frequencies. However, body-generated turbulence (such as that caused by periodic vortex shedding) increases the aerodynamic admittance. Holmes (2001) model is provided in Figure 18, which accounts for only the usually large-scale and small-scale effects.

Figure 18 shows the measured mechanical admittance functions in the along-wind direction for different crown configurations in terrain T1. The mechanical admittance functions reflect background parts caused by the wind and resonant parts caused by the aeroelastic model tree at low and relatively higher frequency, respectively. For $f/f_{crown} < 1$, the admittance is almost constant with values of about 1. This is mainly because there is a highly positive correlation between base overturning moments and wind speeds in the same frequency range, as shown in Figure 14(a). This is the quasi-steady range, where large-scale gusts control the response, consistent with aerodynamic admittance model included in the figure. Here "large-scale" implies gusts larger than U_{ref}/f_{crown}, rather than a typical dimension proportional to a physical dimension. The first peaks appear near the crown natural frequency, while the secondary peaks, which are smaller in magnitude (except for case C2) and narrower in bandwidth, appear near the trunk frequency. This indicates that the crown frequency effectively controls the response via mechanical admittance, which amplifies the response at the crown frequency. However, this effect is slightly reduced as more leaves or branches are added to the tree because of a reduction of peak values in the admittance at $f/f_{crown} = 1$. For smaller scale gusts, with $f/f_{crown} > 1$, the admittance falls off rapidly (except for an increase in values at the trunk frequency), as these smaller gusts do not coherently act on the crown. The fall-off is more rapid than Holmes' model for $f/f_{crown} > 1.5$ which may be due to branches moving out of phase with the bulk of the crown.

6. Conclusions

In this study, the characteristics of base overturning moments, base overturning moment coefficients, and crown deflections were investigated for the aeroelastic model of a tree with eight distinct crown configurations in four terrain conditions. The energy transfer functions for different crown configurations were also examined. The main findings are as follows:

(i) An approach to constructing an aeroelastic model of a tree which satisfies geometric similarity, dynamic similarity and dimensionless parameters including Froude number, Cauchy number and density ratio was developed. Although the model could not include leaf deformation, it captured the major aerodynamic characteristics related to the branch structure.

(ii) Crown sheltering effects of leaves, which effectively limit the increases of crown deflections with increased crown area, occur when there are more than 67% of the leaves (relative to the case C8). Then crown deflections limit the increases of base overturning moment coefficients with increased crown area. In addition, the base overturning moment coefficients decrease with increased wind speeds and increased ABL momentum

thickness, respectively.

(iii) The COV for base overturning moments, moment coefficients and crown deflection in the along-wind direction are determined by turbulence intensity of the wind. Crown frequencies dominate the fluctuations of base overturning moments, moment coefficients, and both crown deflections in the along-wind and across-wind directions for different crown configurations (i.e., number of leaves and branches).

(iv) The energy transfer functions for different crown configurations in the along-wind direction indicate that mechanical admittance presents obvious peaks in the crown frequency, with much smaller peaks in the trunk frequency. The crown responds to large-scale gusts in a quasi-steady manner for gusts larger than U_{ref}/f_{crown}, with dynamic amplification at the crown frequency, and a rapid drop for gusts smaller than U_{ref}/f_{crown}. Increased numbers of branches and leaves reduce the dynamic amplification effect in the crown frequency.

The primary limitations of the current model tree are as follows:

(i) The inflexible leaves clearly affect the streamlining of the crown. Material limitations restrict the accurate simulation of the bending stiffness of lamina and petiole. These limitations should be a focus of future work, although they will remain a challenge.

(ii) The mismatch about integral length scale between wind tunnel terrains and theoretical full-scale terrains causes the discrepancy on swaying behavior between the aeroelastic model tree and the prototype. It would be useful to know if the quasi-steady behavior is maintained for larger integral scales.

(iii) The mismatch on internal damping between the aeroelastic model tree and the prototype also causes the discrepancy on swaying behavior, which affects the application of the results in full scale.

Acknowledgements

This study was funded by the Natural Sciences and Engineering Research Council (NSERC) of Canada under the Discovery Grants program, a donation from ImpactWX to the Northern Tornadoes Project, the National Natural Science Foundation of China [Grant number: 51678233] and China Scholarship Council (CSC). The authors are indebted to Jinlin Xia for his support with the set-up of the wind tunnel tests.

References

Aly, A. M., Fossati, F., Muggiasca, S., et al., 2013. Wind loading on trees integrated with a building envelope. Wind Struct. 17(1), 69-85. DOI: 10.12989/was.2013.17.1.069.

Borisevich, S. A., Vikhrenko, V. S., 2018. Evaluation of the drag coefficients of tree crowns by numerical modeling of their free fall. Agric. For. Meteorol. 256-257, 346-352. DOI: 10.1016/j.agrformet.2018.03.020.

Cao, J., Tamura, Y., Yoshida, A., 2012. Wind tunnel study on aerodynamic characteristics of shrubby specimens of three tree species. Urban For. Urban Green. 11, 465-476. DOI: 10.1016/j.ufug.2012.05.003.

Davenport, A. G., 1961. The buffeting of structures by gusts. Proceedings, International Conference on Wind Effects on Buildings and Structures, Teddington U.K., 358-91.

ESDU, 2008a. Characteristics of Atmospheric Turbulence Near the Ground. Part II: Single point Data for strong Winds (Neutral Atmosphere) (ESDU 85020). Engineering Sciences Data Unit, London, UK.

Gardiner, B. A., 1994. Wind and wind forces in a plantation spruce forest. Bound.-Layer Meteor. 64, 161-186. DOI: 10.1007/BF00705512.

Giammanco, I. M., Schroeder, J. L., Masters, F. J., et al., 2016. Influence on observed near-surface gust factors in landfalling U.S. gulf coast hurricanes: 2004-08. J. Appl. Meteorol. Climatol. 55, 2587-2611. DOI: 10.1175/JAMC-D-16-0053.1.

Gillies, J. A., Lancaster, N., Nickling, W. G., et al., 2000. Field determination of drag forces and shear stress partitioning effects for a desert shrub (Sarcobatus vermiculatus, greasewood). J. Geophys. Res.-Atmos. 105, 24871-24880. DOI: 0148-0227/00/2000JD900431.

Gillies, J. A., Nickling, W. G., King, J., 2002. Drag coefficient and plant form response to wind speed in three plant species: Burning Bush (Euonymus alatus), Colorado Blue Spruce (Picea Pungens glauca.), and Fountain Grass (Pennisetum setaceum). J. Geophys. Res.-Atmos. 107, 1-15. DOI: 0148-0227/02/2001JD001259.

Gonzales, H. B., Casada, M. E., Hagen, L. J., et al., 2018. Porosity and drag determination of a single-row vegetative barrier (maclura pomifera). Trans. ASABE. 61(2), 641-652. DOI: 10.13031/trans.12338.

Grant, P. F., Nickling, W. G., 1998. Direct filed measurement of wind drag on vegetation for application to windbreak design and modelling. Land Degrad. Dev. 9, 57-66. DOI: 1085-3278/98/010057-10.

Gromke, C., Ruck, B., 2008. Aerodynamic modelling of trees for small-scale wind tunnel studies. Forestry. 81, 243-258. DOI: 10.1093/forestry/cpn027.

Gromke, C., 2018. Wind tunnel model of the forest and its Reynolds number sensitivity. J. Wind Eng. Ind. Aerodyn. 175, 53-64. DOI: 10.1016/j.jweia.2018.01.036.

Guan, D., Zhang, Y., Zhu, T., 2003. A wind-tunnel study of windbreak drag. Agric. For. Meteorol. 118, 75-84. DOI: 10.1016/S0168-1923(03)00069-8.

Holmes, J. D., 2001. Wind loading of structure, first ed. Spon, Canada.

Hu, W., Gao, H., Jiang, X., et al., 2012. Analysis on constituents and contents in leaf essential oil from three chemical types of Cinnamum camphor. Journal of Central South University of Forestry & Technology. 32(11): 186-194 (in Chinese).

James, K. R., 2010. A dynamic structural analysis of trees subjected to wind loading. PhD thesis, Melbourne School of Land and Environments, The University of Melbourne.

Jiang, Z., Peng, Z., 2001. Wood properties of the global important tree species. Science Press, Beijing, China (in Chinese).

Kane, B., Smiley, E. T., 2006. Drag coefficients and crown area estimation of red maple. Can. J. For. Res. 36, 1951-1958. DOI: 10.1139/X06-086.

Kane, B., Pavlis, M., Harris, J. R., et al., 2008. Crown reconfiguration and trunk stress in deciduous trees. Can. J. For. Res. 38, 1275-1289. DOI: 10.1139/X07-225.

Kitagawa, K., Iwama, S., Fukui, S., et al., 2015. Effects of components of the leaf area distribution on drag relations for Cryptomeria japonica and Chamaecyparis obtusa. Eur. J. Forest Res. 134, 403-414. DOI: 10.1007/s10342-014-0859-6.

Koizumi, A., Motoyama, J., Sawata, K., et al., 2010. Evaluation of drag coefficients of poplar-tree crowns by a field test method. J. Wood Sci. 56, 189-193. DOI: 10.1007/s10086-009-1091-8.

Koizumi, A., Shimizu, M., Sasaki, Y., et al., 2016. In situ drag coefficient measurements for rooftop trees. J. Wood Sci. 62, 363-369. DOI: 10.1007/s10086-016-1556-5.

Mayhead, G. J., 1973. Some drag coefficients for British forest trees derived from wind tunnel studies. Agric. Meteorol. 12, 123-130. DOI: 10.1016/0002-1571(73)90013-7.

Miller, C., Balderrama, J. A., Masters, F. J., 2015. Aspects of observed gust factors in landfalling tropical cyclones: gust components, terrain, and upstream fetch effects. Bound.-Layer Meteor. 155, 129-155. DOI: 10.1007/s10546-014-9989-0.

Moore, J. R., Maguire, D. A., 2004. Natural sway frequencies and damping ratios of trees: concepts, review and synthesis of previous studies. Trees-Struct. Funct. 18, 195-203. DOI: 10.1007/s00468-003-0295-6.

Moore, J. R., Maguire, D. A., 2008. Simulating the dynamic behavior of Douglas-fir trees under applied loads by the finite element method. Tree Physiol. 28, 75-83. DOI: 10.1093/treephys/28.1.75.

Reynders, E., Degrauwe, D., Roeck, G. D., et al., 2010. Combined experimental-operational modal testing of footbridges. J. Eng. Mech. 136(6), 687-696. DOI: 10.1061/(ASCE)EM.1943-7889.0000119.

Robertson, A., 1987. The centroid of tree crowns as an indicator of abiotic processes in a balsam fir wave forest. Can. J. For. Res. 17, 746-755. DOI: 10.1139/x87-119.

Rudnicki, M., Mitchell, S. J., Novak, M. D., 2004. Wind tunnel measurements of crown streamlining and drag relationships for three conifer species. Can. J. For. Res. 34, 666-676. DOI: 10.1139/X0.-233.

Schindler, D., Vogt, R., Fugmann, H., et al., 2010. Vibration behavior of plantation-grown Scots pine trees in response to wind excitation. Agric. For. Meteorol. 150, 984-993. DOI: 10.1016/j.agrformet.2010.03.003.

Sergio, C. G., Gregorio, L. B. R., Jesus, A. G. R., et al., 2008. Dynamic analysis of olive trees in intensive orchards under forced vibration. Trees. 22, 795-802. DOI: 10.1007/s00468-008-0240-9.

Stacey, G. R., Belcher, R. E., Wood, C. J., et al., 1994. Wind flows and forces in a model spruce forest. Bound.-Layer Meteor. 69, 311-334. DOI: 10.1007/BF00708860.

Tanaka, N., Takenaka, H., Yagisawa, J., et al., 2011. Estimation of drag coefficient of a real tree considering the vertical stand structure of trunk, branches, and leaves. Intl. J. River Basin Management. 9, 221-230. DOI: 10.1080/15715124.2011.606427.

Taylor, Z. J., Gurka, R., Kopp, G. A., Liberzon, A., 2010. Long-duration time-resolved PIV to study unsteady aerodynamics. IEEE Trans. Instrum. Meas. 59, 3262–3269. DOI: 10.1109/TIM.2010.2047149.

Vogel, S., 1989. Drag and reconfiguration of broad leaves in high winds. J. Exp. Bot. 40, 941-948. DOI: 10.1093/jxb/40.8.941.

Vollsinger, S., Mitchell, S. J., Byrne, K. E., et al., 2005. Wind tunnel measurements of crown streamlining and drag relationships for several hardwood species. Can. J. For. Res. 35, 1238-1249. DOI: 10.1139/X05-051.

Figures

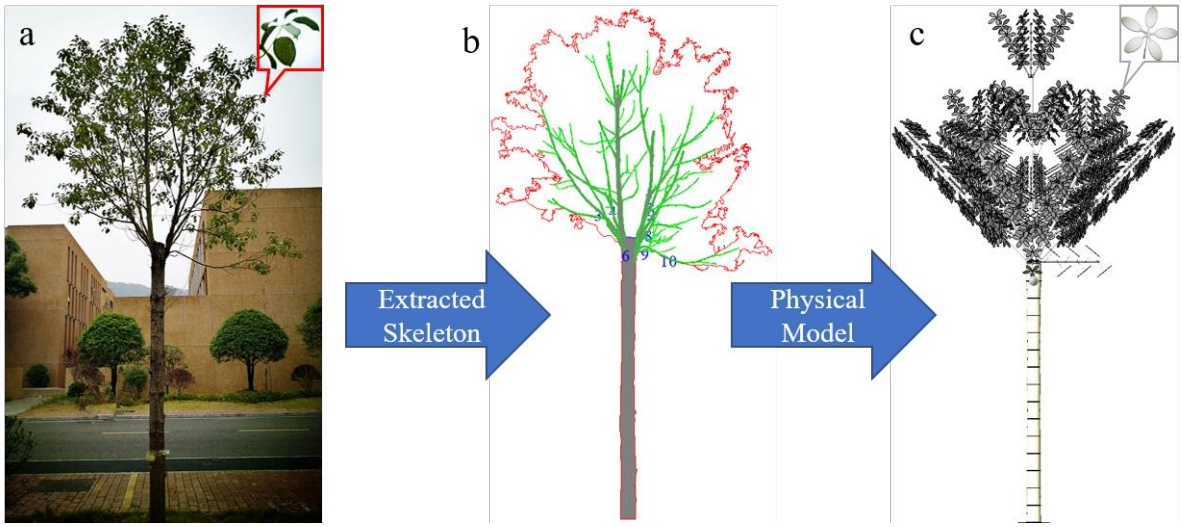

Figure 1: Schematic of the aeroelastic model tree: (a) prototype, (b) skeleton and (c) model.

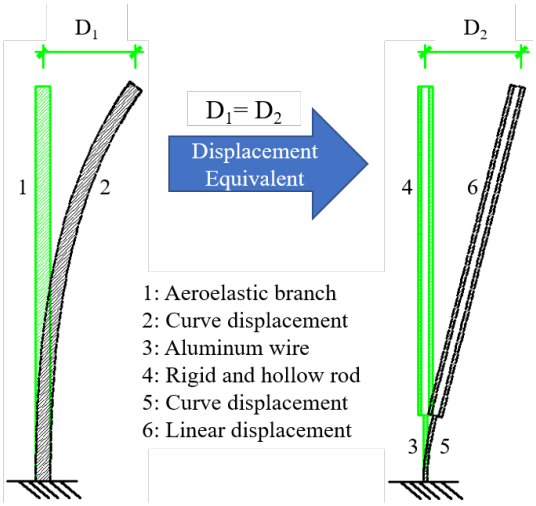

Figure 2: Schematic of equivalent displacement for the free ends of branches

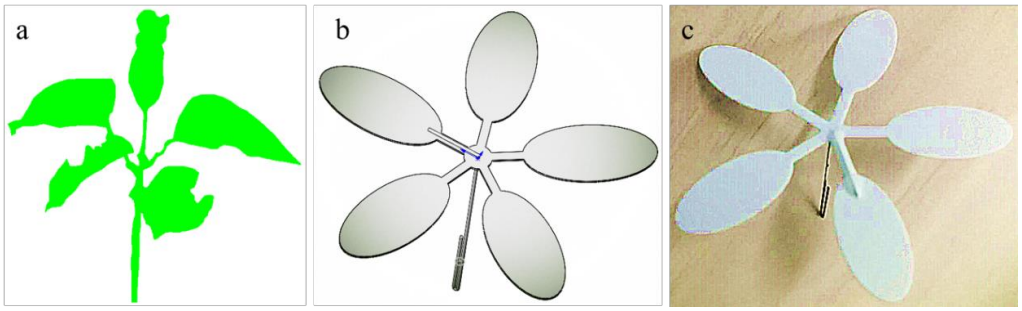

Figure 3: Leaf cluster: (a) prototype, (b) 3D computer model and (c) actual model.

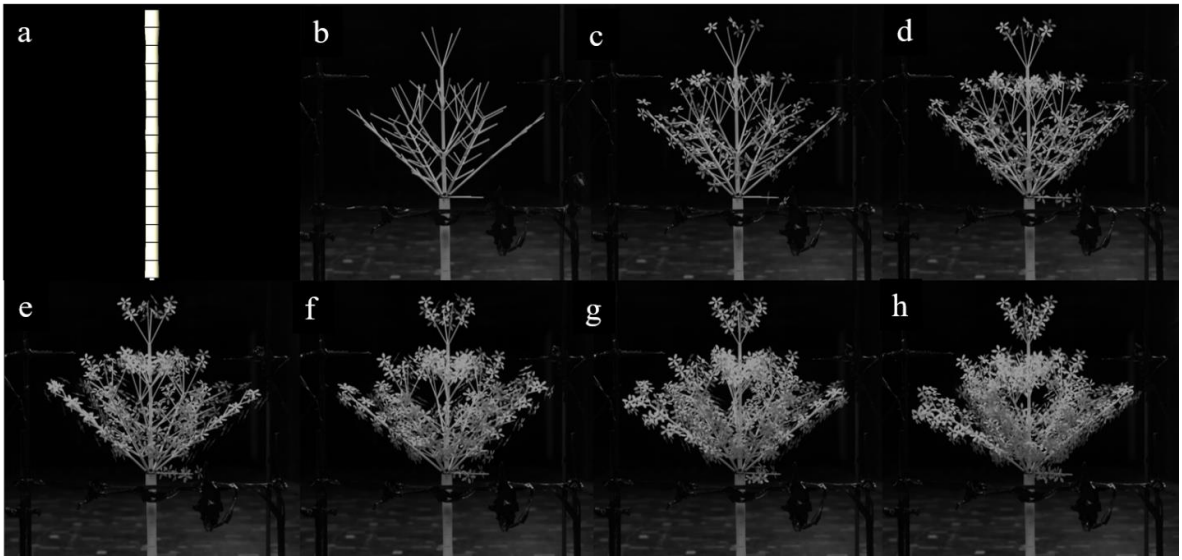

Figure 4: Eight configurations, C1 (a), C2 (b), C3 (c), C4 (d), C5 (e), C6 (f), C7 (g) and C8 (h).

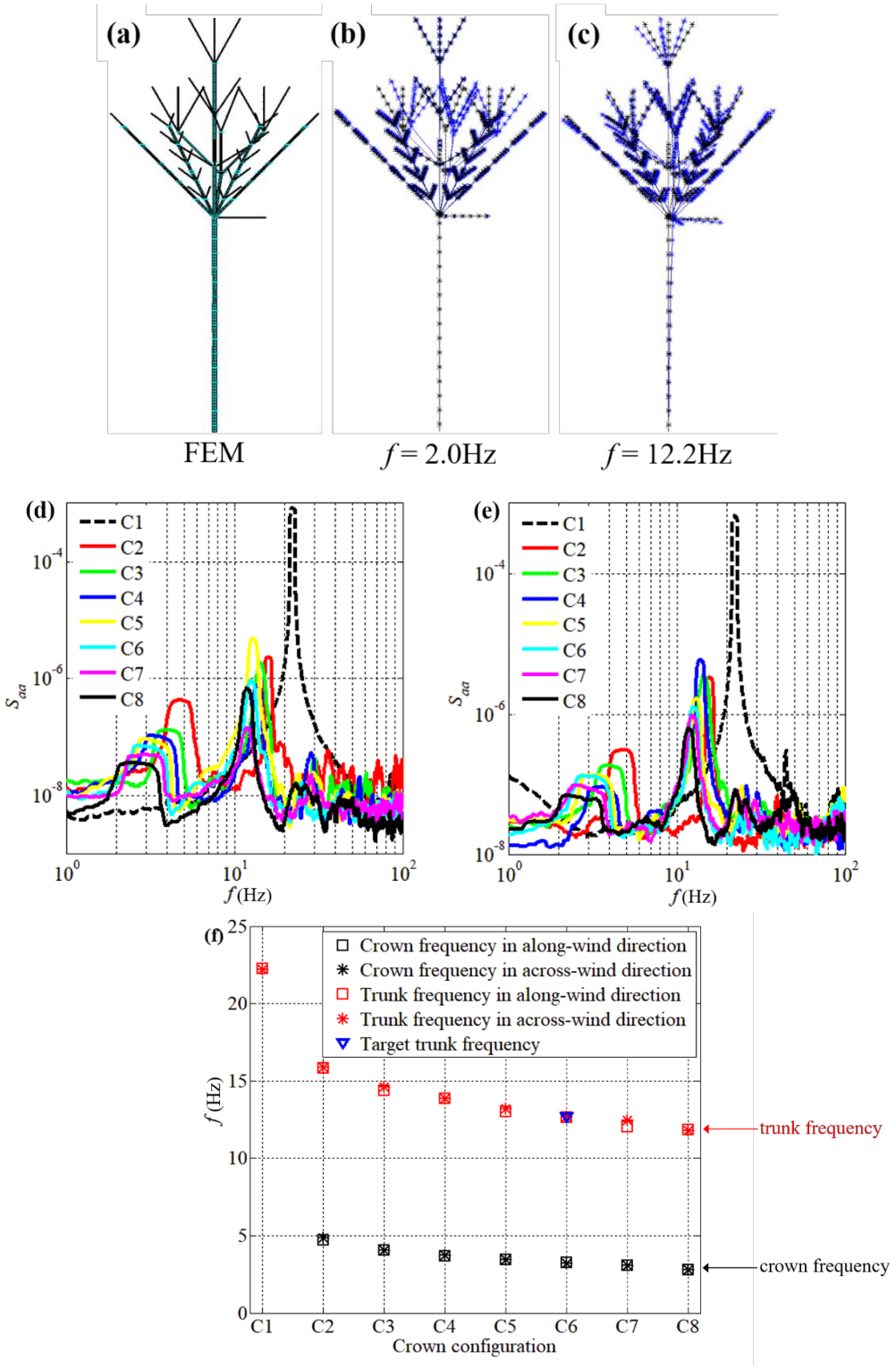

Figure 5: (a) FEM of the aeroelastic model tree, mode shapes corresponding to (b) crown and (c) trunk frequencies for case C8, power spectral density functions of accelerations at the top of the trunk for different configurations in the (d) along-wind and (e) across-wind directions derived from free vibration decay tests, and (f) frequencies of the aeroelastic model tree in the along-wind and across-wind directions.

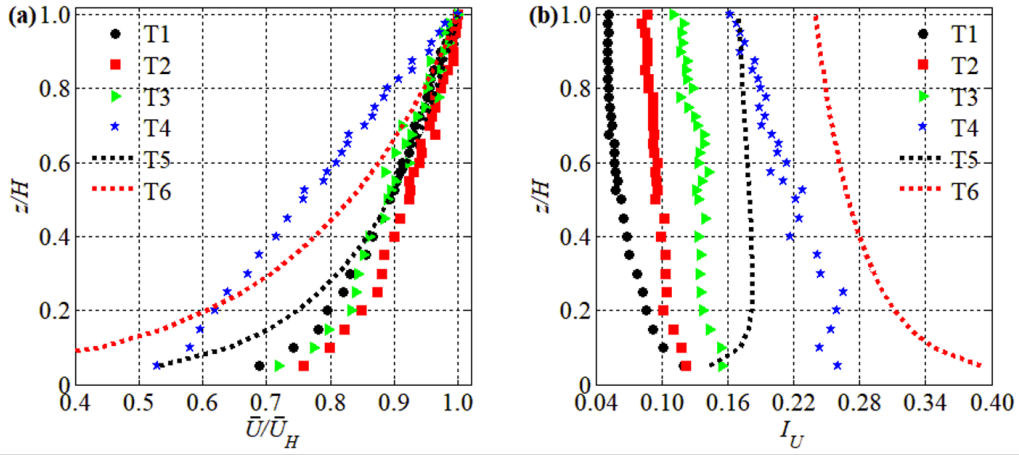

Figure 6: (a) Non-dimensional mean velocity profiles normalized by the mean velocity at the top of tree and (b) turbulence intensity profiles for four wind tunnel terrains (T1, T2, T3, T4), and two theoretical full-scale terrains named as “Open” and “Suburban” (T5, T6).

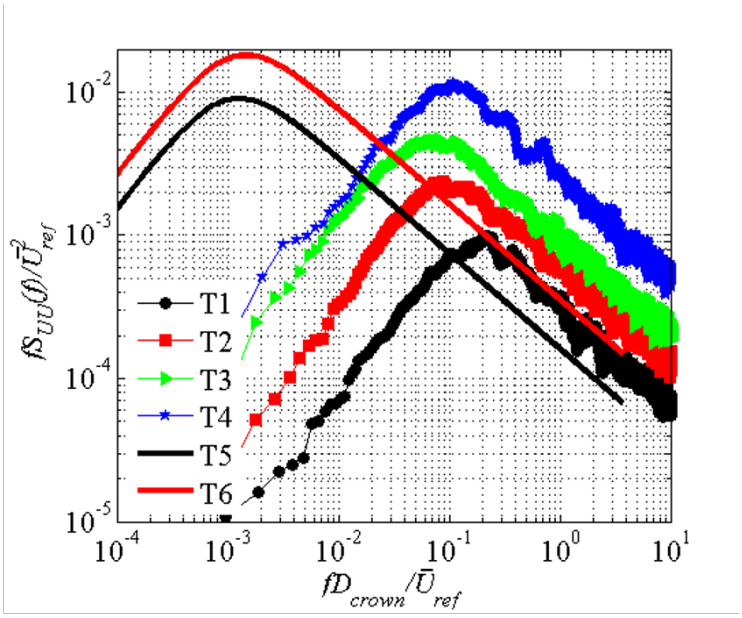

Figure 7: Power spectral density functions of streamwise velocities at reference height in four wind tunnel terrains (T1, T2, T3, T4, $z_{ref} = 0.85\text{m}$), and two theoretical full-scale terrains named as "Open" and "Suburban" (T5, T6, $z_{ref} = 5.1\text{m}$).

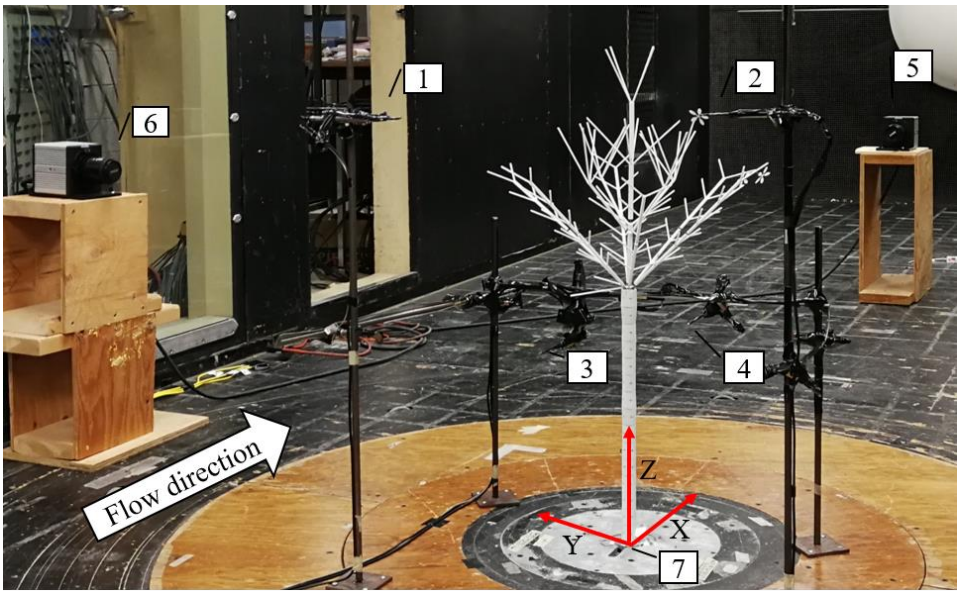

Figure 8: The set-up of the wind tunnel tests: 1 cobra probe 1 (-0.22, 0.36, 0.85)，2 cobra probe 2 (-0.22, -0.25, 0.85), 3 cobra probe 3 (-0.075, 0.15, 0.35), 4 cobra probe 4 (-0.075, -0.15, 0.35), 5 downstream camera (2.8, 0, 0.65), 6 lateral camera (0.05, 1.35, 0.65), 7 JR3 force balance (0, 0, -0.025). (X, Y, Z), unit: m.

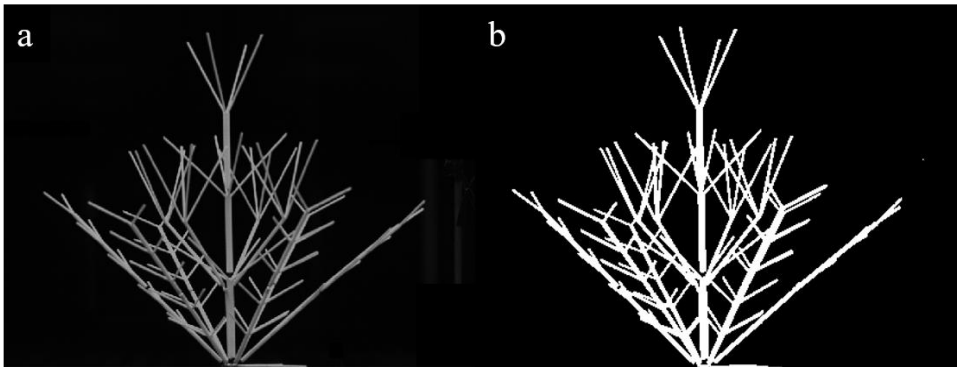

Figure 9: Frontal area of the aeroelastic model tree, (a) cropped image, (b) spatially discretized image.

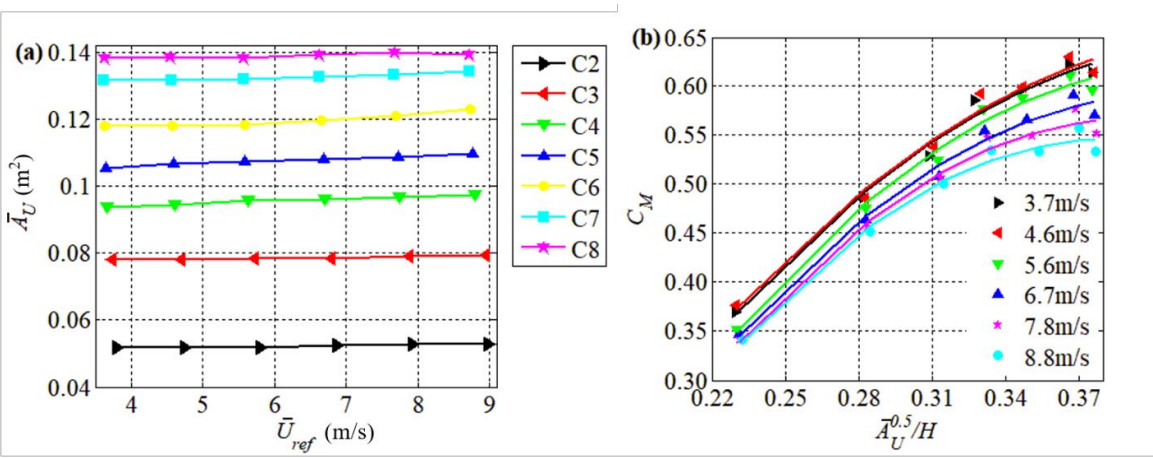

Figure 10: (a) Variations of mean frontal areas ($\bar{A}_U$) versus mean reference wind speeds ($\bar{U}_{ref}$) for cases C2 to C8, (b) variations of mean base overturning moment coefficients ($\bar{C}_M$) versus square roots of mean frontal areas divided by the height of the model tree ($\bar{A}_U^{0.5}/H$) at reference wind speeds of 3.7 m/s to 8.8 m/s in T1.

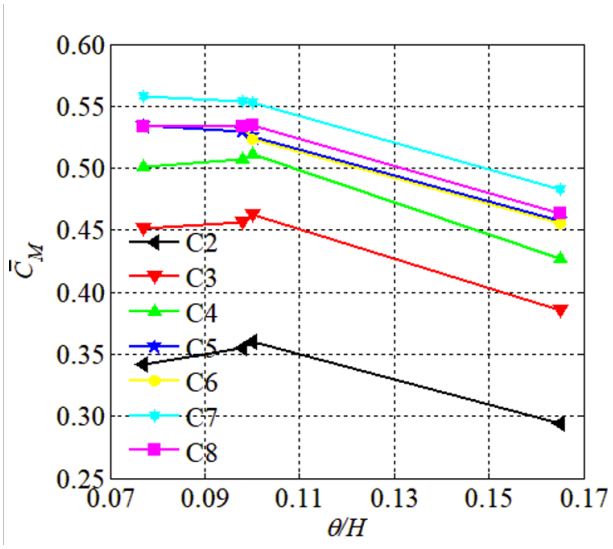

Figure 11: Variations of mean base overturning moment coefficients ($\bar{C}_M$) versus momentum thickness normalized by the height of the model tree (θ/H) for cases C2 to C8 at a reference wind speed of 8.8 m/s, for terrains T1, T2, T3 and T4.

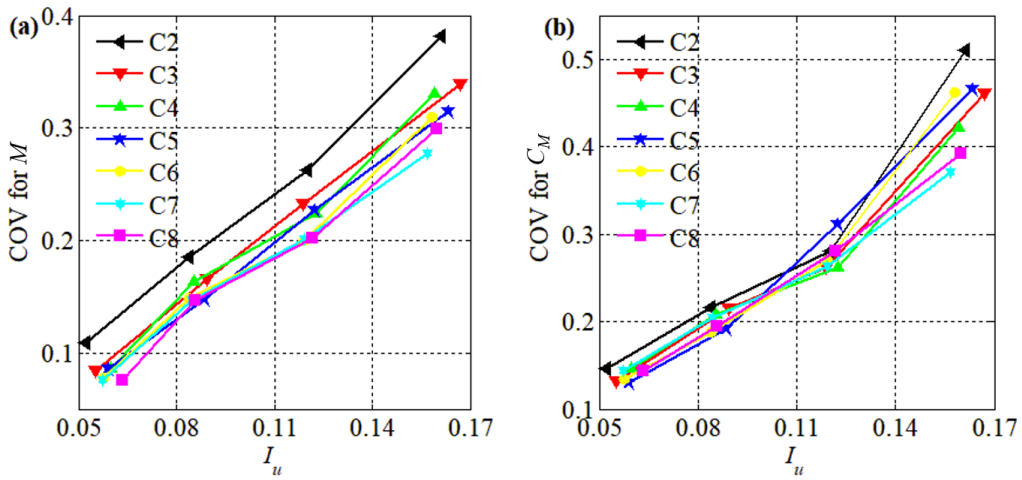

Figure 12: Variations of COV for (a) base overturning moment (M) and (b) moment coefficients (C_M) versus turbulence intensity (I_U) for cases C2 to C8 at a reference wind speed of 8.8 m/s, for terrains T1, T2, T3 and T4.

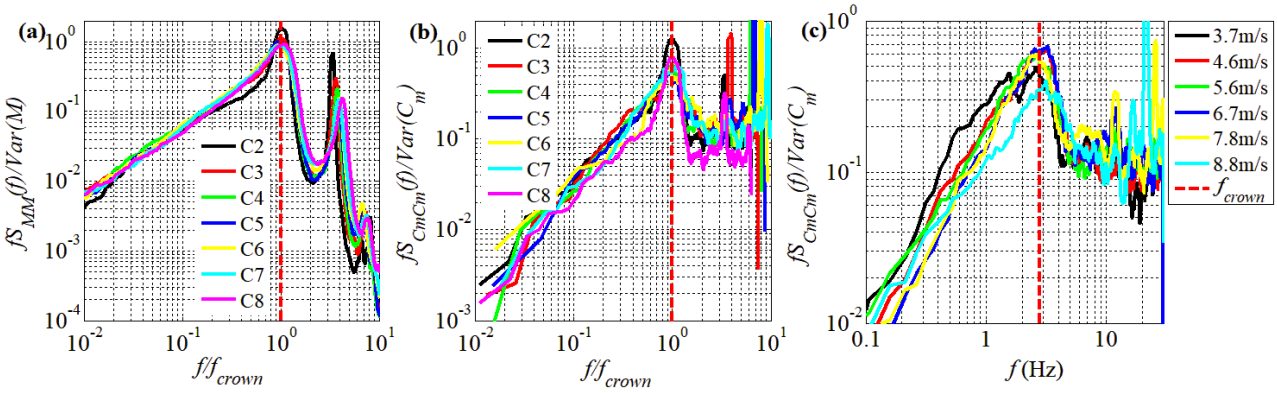

Figure 13: Power spectral density functions of (a) base overturning moments and (b) base overturning moment coefficients versus frequency normalized by crown frequency (f/f_{crown}) for cases C2 to C8 in the along-wind direction at reference wind speed of 8.8 m/s, and (c) base overturning moment coefficients versus frequency for case C8 in the along-wind direction at reference wind speeds of 3.7 m/s to 8.8 m/s in T1.

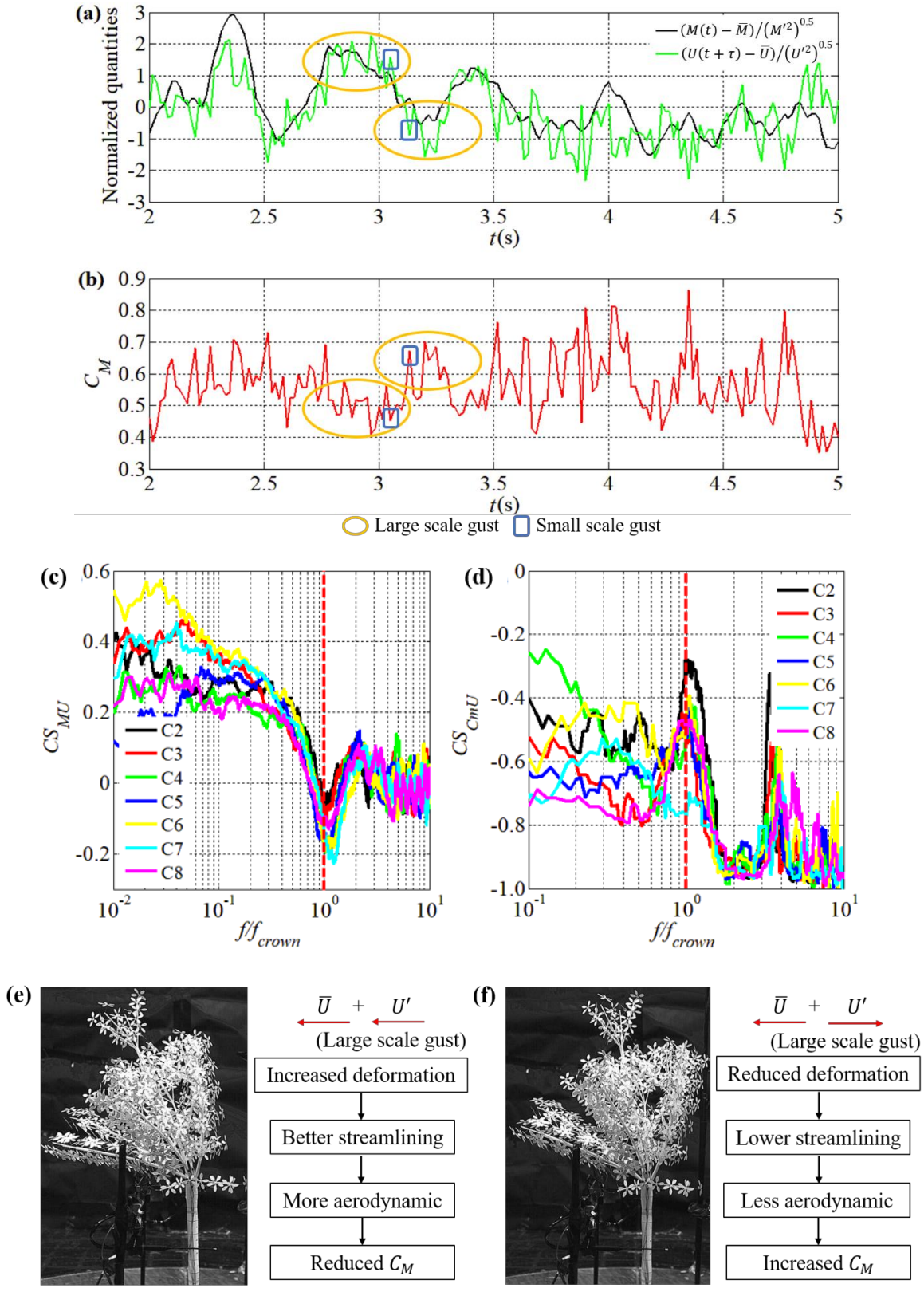

Figure 14: Time history of (a) normalized base overturning moment ($(M(t)-\bar{M})/(M'^2)^{0.5}$) and normalized reference wind speed ($(U(t+\tau)-\bar{U})/(U'^2)^{0.5}$), and (b) base overturning moment coefficient ($C_M(t)=$

$(M(t) - m_{crown} * d_{cc})/(0.5 * \rho * U_{ref}(t+\tau)^2 * A_U(t) * H)$) for case C8, normalized co-spectral density functions between (c) base overturning moments and reference wind speeds, and (d) base overturning moment coefficients and reference wind speeds versus frequency normalized by crown frequency (f/f_{crown}) for cases C2 to C8, and crown deformation with (e) positive and (f) negative large scale gusts for case C8, at reference wind speed of 8.8 m/s in T1.

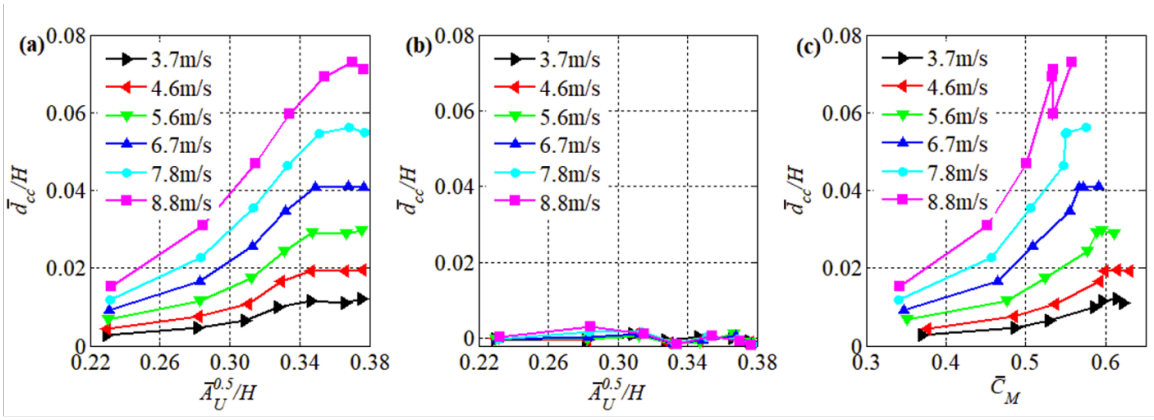

Figure 15: Variations of mean crown center displacements ($\bar{d}_{cc}/H$) in the (a) along-wind and (b) across-wind directions versus square roots of mean frontal areas divided by the height of the model tree ($\bar{A}_U^{0.5}/H$), and (c) mean crown center displacements ($\bar{d}_{cc}/H$) in the along-wind direction versus base overturning moment coefficients ($\bar{C}_M$) at reference wind speeds of 3.7 m/s to 8.8 m/s in T1.

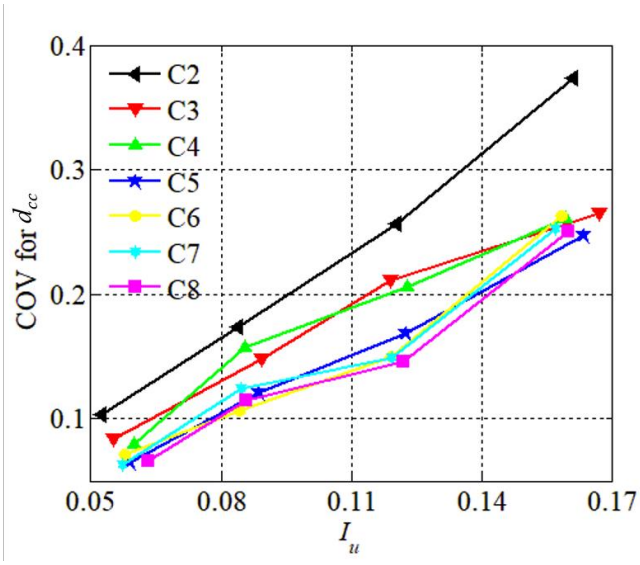

Figure 16: Variations of COV for crown center displacement (d_{cc}) in the along-wind direction versus turbulence intensity (I_U) for cases C2 to C8 at a reference wind speed of 8.8 m/s, for terrains T1, T2, T3 and T4.

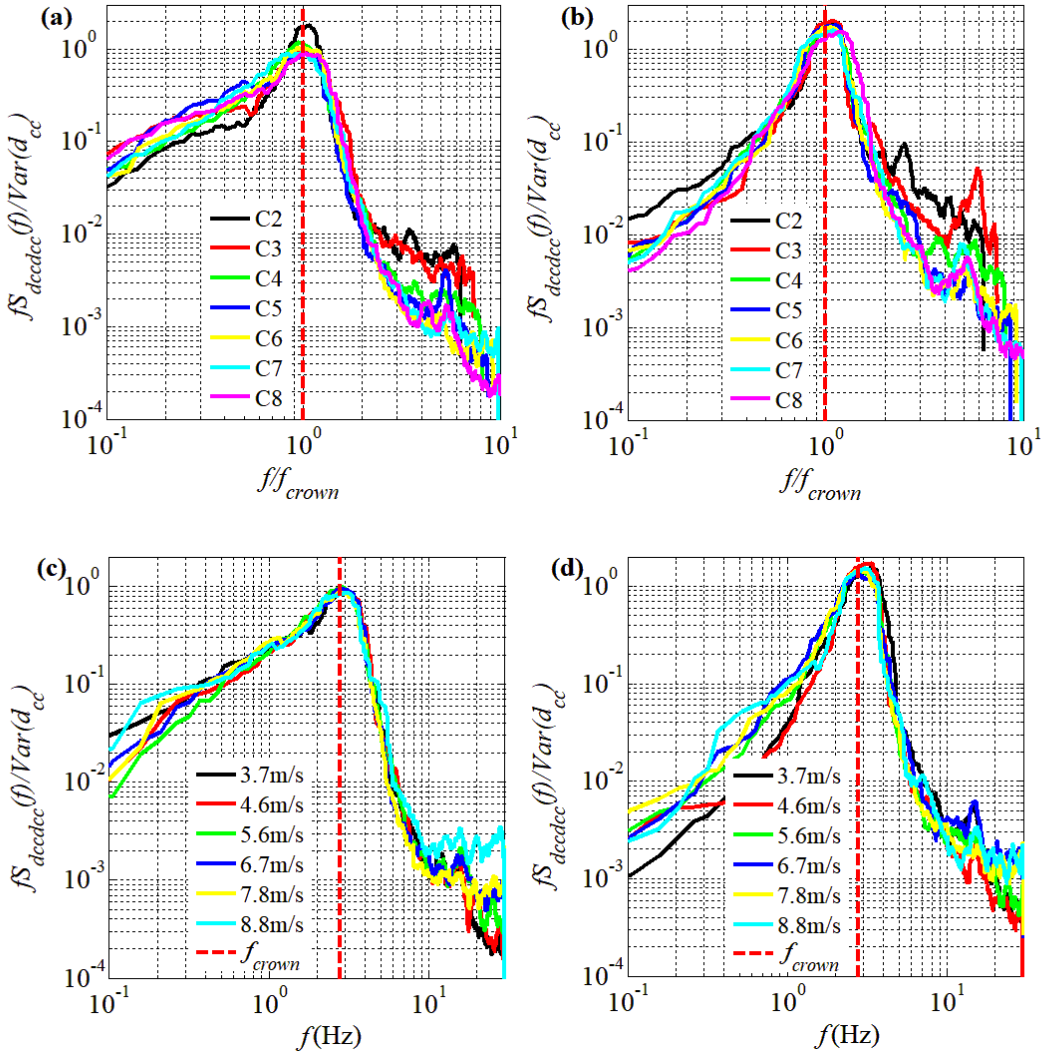

Figure 17: Power spectral density functions of crown center displacements in the (a) along-wind and (b) across-wind directions versus frequency normalized by crown frequency (f/f_{crown}) for cases C2 to C8 at reference wind speed of 8.8 m/s, and in the (c) along-wind and (d) across-wind directions versus frequency for case C8 at reference wind speeds of 3.7 to 8.8 m/s in T1.

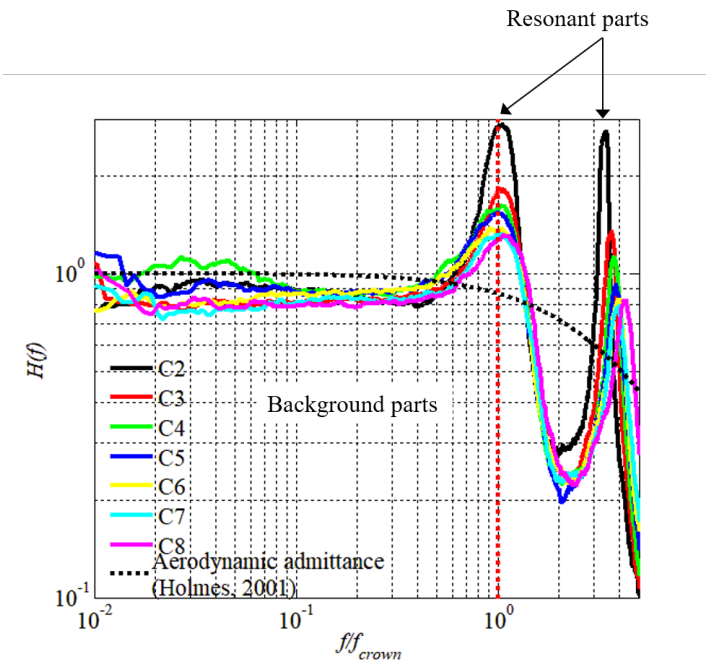

Figure 18: Mechanical admittance functions versus frequency normalized by crown frequency (f/f_{crown}) for cases C2 to C8 in the along-wind direction at reference wind speed of 8.8 m/s in T1.

Tables

Table 1: Aeroelastic scaling parameters

Parameter	Unit	Reduced ratio	Similarity requirement
Length	m	$\lambda_L = 1:6$	Wind tunnel scale
Velocity	m/s	$\lambda_U = 1:2.45$	Froude number
Density	kg/m^3	$\lambda_\rho = 1:1$	$\lambda_\rho = \rho_m/\rho_p$
Frequency	Hz	$\lambda_f = 2.45:1$	$\lambda_f = \lambda_U/\lambda_L$
Time	s	$\lambda_t = 1:2.45$	$\lambda_t = \lambda_L/\lambda_U$
Mass per meter	kg/m	$\lambda_m = 1:6^2$	$\lambda_m = \lambda_\rho \lambda_L^2$
Mass Moment of Inertia per meter	$kg \cdot m^2/m$	$\lambda_j = 1:6^4$	$\lambda_j = \lambda_m \lambda_L^2$
Bending Stiffness	$N \cdot m^2$	$\lambda_{EI} = 1:(2.45^2 \cdot 6^4)$	$\lambda_{EI} = \lambda_U^2 \lambda_L^4$ Cauchy number

Table 2: Dimensions and mass for the aeroelastic model tree without wind

Configuration	Tree height(m)	Crown height(m)	Tree mass(kg)	Frontal area(m^2)	Crown area(m^2)
C1	0.50	0.00	0.1568	0.0135	0.0000
C2	0.96	0.46	0.2587	0.0516	0.0381
C3	0.99	0.49	0.2759	0.0775	0.0640
C4	0.99	0.49	0.2941	0.0924	0.0789
C5	0.99	0.49	0.3122	0.1035	0.0900
C6	0.99	0.49	0.3297	0.1162	0.1027
C7	0.99	0.49	0.3470	0.1310	0.1175
C8	0.99	0.49	0.3657	0.1366	0.1231

Table 3: Characteristics of the four wind tunnel terrains and two theoretical full-scale terrains

Terrain	Turbulence intensity, I_u	Integral scale, L_x	Momentum thickness,θ
	$z_{ref} = 0.85H$	L_x/D_{crown} $z_{ref} = 0.85H$	θ/H
T1	0.051	0.76	0.100
T2	0.088	1.68	0.077
T3	0.12	2.02	0.098
T4	0.19	1.35	0.165
T5	0.17	19.58	0.107
T6	0.25	16.93	0.136

Table 4: Characteristics of reference wind speeds, base overturning moments, damping, base overturning moment coefficients and crown deflections for cases C2 to C8 at reference wind speed of 8.8 m/s in T1.

Configuration		C2	C3	C4	C5	C6	C7	C8
Reference wind speed in the along-wind direction U_{ref} (m/s)	mean	8.98	8.95	8.80	8.76	8.73	8.72	8.73
	SD	0.47	0.49	0.53	0.52	0.50	0.50	0.55
	COV	0.053	0.055	0.060	0.059	0.058	0.057	0.063
Base overturning moment in the along-wind direction M (N.m)	mean	0.8698	1.7119	2.2463	2.6855	2.9822	3.3976	3.3775
	SD	0.1035	0.1541	0.2065	0.2468	0.2502	0.2751	0.2743
	COV	0.1190	0.0900	0.0919	0.0919	0.0839	0.0810	0.0812
Damping in the along-wind direction (%)	structural and aerodynamic damping	6.1	5.6	6.3	5.0	4.0	6.1	3.2
Base overturning moment coefficient in the along-wind direction C_M	mean	0.3416	0.4513	0.5007	0.5348	0.5337	0.5579	0.5339
	SD	0.0532	0.0609	0.0761	0.0723	0.0732	0.083	0.0797
	COV	0.1557	0.1349	0.1520	0.1352	0.1372	0.1488	0.1493
Crown deflection in the along-wind direction d_{cc}(m)	mean	0.0150	0.0305	0.0464	0.0590	0.0685	0.0721	0.0704
	SD	0.0016	0.0026	0.0037	0.0039	0.0049	0.0045	0.0046
	COV	0.1067	0.0852	0.0797	0.0661	0.0715	0.0624	0.0653
Crown deflection in the across-wind direction d_{cc}(m)	mean	0.0003	0.0029	0.0011	0.0016	0.0007	0.0006	0.0018
	SD	0.0010	0.0015	0.0020	0.0029	0.0027	0.0033	0.0035
	COV	3.3333	0.5172	1.8182	1.8125	3.8571	5.5000	1.9444

SD is standard deviation, COV is coefficient of variation, mean = mean (•), SD = std (•), and COV = SD / mean.